PERGAMON

International Journal of Solids and Structures 40 (2003) 5973–5999

INTERNATIONAL JOURNAL OF SOLIDS and STRUCTURES

www.elsevier.com/locate/ijsolstr

Craft—a plastic-damage-contact model for concrete. I. Model theory and thermodynamic considerations

A.D. Jefferson *

Division of Civil Engineering, Cardiff University, P.O. Box 925, CF24 0YF Cardiff, UK

Received 31 January 2003; received in revised form 16 June 2003

Abstract

A framework is described for the development of a thermodynamically consistent plastic directional-damage-contact model for concrete. This framework is used as a basis for a new model, named Craft, which uses planes of degradation that can undergo damage and separation but which can regain contact according to a contact state function. The thermodynamic validity of the resulting model is considered in detail, and is proved for certain cases and demonstrated numerically for others. The model has a fully integrated plasticity component that uses a smooth triaxial yield surface and frictional hardening–softening functions. A new type of consistency condition is introduced for simultaneously maintaining both local and global constitutive relationships as well as stress transformation relationships. The introduction of contact theory provides the model with the ability to simulate the type of delayed aggregate interlock behavior exhibited by fully open crack surfaces that subsequently undergo significant shear movement. The model has been implemented in a constitutive driver program as well as a finite element program. The model is assessed against a range of experimental data, which includes data from uniaxial tension tests with and without unloading–reloading cycles, tests in which cracks are formed and then loaded in shear, and uniaxial, biaxial and triaxial compression tests.

Keywords: Constitutive; Damage; Fracture; Plasticity; Concrete

1. Introduction

Numerical modeling of concrete is a mature discipline with a history that spans more than three decades, during which time considerable advances have been made in both the underlying theories of the constitutive models as well as in the practical capabilities of finite and boundary element codes for concrete analysis. Given the vast body of literature produced on this subject, the need for further contributions could be reasonably questioned. However, since research on the subject has not yet resulted in a model, or set of models, which is able to represent the complete range of concrete characteristic behavior in a consistent and robust manner, the author believes that present and future strivings towards the goal of a comprehensive and robust set of numerical models for concrete are, and will be for some time to come, justified.

* Tel.: +44-29-2087-4263; fax: +44-29-2087-4597.
E-mail address: jeffersonad@cf.ac.uk (A.D. Jefferson).

0020-7683/$ - see front matter © 2003 Elsevier Ltd. All rights reserved.
doi:10.1016/S0020-7683(03)00390-1

During the period referred to there have been two particular state-of-the-art reviews that have described many of the key developments up to their date of publication (ASCE, 1982; ACI, 1998). Included in these reviews are descriptions of a class of model that received much attention in the 1970s and 1980s (Buyukozturk, 1977; Owen et al., 1983; de Borst, 1986; Cervera et al., 1987). These models, which will be termed here 'plastic-cracking', used plasticity theory to represent the compressive behavior of concrete and various total and incremental fracture theories to simulate directional cracking on defined planes. There was considerable variation in the plasticity and fracture components of these models, although the underlying principles were similar. The approaches used to model cracking—which included the fixed crack, rotating crack and multi-non-orthogonal fixed crack methods—have been reviewed in two publications (Weihe et al., 1998; Petrangeli and Ozbolt, 1996). This type of plastic-cracking model is appealing for a number of reasons; firstly, the behavior of concrete in compression is naturally and accurately simulated with plasticity theory. This is because, for a wide range of uniaxial, biaxial and triaxial stress/strain paths, the inelastic strains are permanent and therefore the unloading behavior is substantially elastic, and the behavior is thereby in agreement with the assumptions of standard plasticity theory. This observation is borne out by the data and simulations of Este and Willam (1994). Secondly, regarding crack modeling, the simulation of directional cracking as strength loss on defined planes agrees with macroscopic observations of crack formation. Furthermore, the author would contend that the approach is also reasonable for simulating the behavior observed during tensile micro-cracking, as, for example, seen in micro-imaging studies reported by van Mier (1997) and Karihaloo and Jefferson (2001), although it is recognized that because the model is phenomenological in nature, and not based on the micro-structure of the material, it will only simulate the macroscopic effects of micro-cracking in an approximate manner. These earlier models were in various ways flawed. The fixed crack approach produced over stiff results and relies on a somewhat arbitrary shear retention factor (Crisfield and Wills, 1989). The rotating crack model can not simulate post crack shear response on a crack plane and also relies on the questionable device of computing Poisson's ratio from current stress and strain components such that the coaxiality of the principal stresses and strains is maintained (Rots, 1988; Petrangeli and Ozbolt, 1996; Feenstra and de Borst, 1995). The disadvantages of the multiple non-orthogonal crack theory, which is in many respects the most appealing of the approaches, have been summarized by Feenstra and de Borst (1995). These disadvantages relate to the computational and algorithmic difficulties associated with combining plasticity and fracture and the problems of simulating state changes, e.g. crack closure.

None of the models referred to above were explicitly developed within thermodynamically consistent theoretical frameworks and certain aspects of the model formulations were rather ill-defined. This is not surprising since, at the time many of these models were developed, appropriate theoretical frameworks for combining the fracture and plasticity components of such models were in an early stage of development. The situation is now quite different due to the major developments in constitutive theories that have occurred over the past twenty years. The developments include new damage based models and theories (Krajcinovic, 1996; di Prisco and Mazars, 1996; Comi and Perego, 2001), advanced plasticity based models for general concrete behavior (Yang et al., 1985; Han and Chen, 1987; Este and Willam, 1994) and for cracking behavior (Feenstra and de Borst, 1995), formulations for combining plasticity and damage (Ortiz, 1985; Simo and Ju, 1987; Hansen and Schreyer, 1994; Ekh and Runesson, 2000), plastic-damage models (Klisinski and Mroz, 1988; Lubiner et al., 1989; Abu-Lebeh and Voyiadjis, 1993; Luccioni et al., 1996; Lee and Fenves, 1998; Meschke et al., 1998; Carol et al., 2001a,b) and the development of the micro-plane model (Bazant et al., 2000; Carol et al., 2001b; Ožbolt et al., 2001). Also Armero and Oller (2000) have considered conditions for the thermodynamic validity of models with directional damage surfaces, which is of particular relevance to the present work. It is noted that there are many other valuable contributions not included in this list, but many are included in a wide ranging recent review paper on plasticity and damage, in which there is particular reference to non-local formulations, by Bazant and Jirasek (2002).

Within many of the above publications there is recognition that both plasticity and damage are required to simulate concrete behavior well, but the complexity of simulating key characteristics of concrete behavior such as increasing deviatoric strength with increasing triaxial confinement, non-linear behavior in compression, loss of tensile strength with compressive crushing, softening in tension leading to the formation of fully formed stress-free cracks, aggregate interlock on partially and fully formed cracks, crack opening and closing with both shear and normal crack surface movements, all within the same framework means that no one model is yet able to simulate well all of these characteristics.

In some respects the older plastic-cracking models had, at least nominally, greater success at simulating certain of the above characteristics than many of the new models, yet the theoretical and practical flaws have understandably led to little work being carried out on them in recent years. However, the author believes that a model that employs modern plastic-damage theory and yet retains certain of the features of the early plastic-cracking models is an attractive proposition; not least because such models work with defined crack planes and therefore have the potential to simulate crack opening and closing behavior and post-crack shear behavior on fully formed crack planes accurately. Furthermore, if a transition to a discrete crack is desired, the crack plane orientation and state variables are directly available, although it is recognized that the process of transferring properties to discrete cracks, when multiple cracks are involved, may be problematic. The development of such a model is subject of this paper.

A thermodynamically consistent framework is described and this is used as a basis for a new model, although as may be seen later, it did not prove possible to derive analytical proofs of thermodynamic consistency for absolutely all cases. The damage, or contact, matrix is generated from planes of degradation (POD is terminology from Weihe et al., 1998), each of which is formed when a damage criterion is satisfied. The POD aspect of the model employs some of the transformation relationships and theory of earlier non-orthogonal crack models (de Borst and Nauta, 1985; Rots, 1988); however, the new model is quite different in that it is developed in a formal plastic-damage-contact (p-d-c) framework, properly couples the response of all PODs via a new consistency condition that enforces the total and local governing constitutive equations and employs a new crack plane model which simulates normal and shear degradation as well as crack closure effects. The fracture aspect of the model is fully integrated with a hardening/softening frictional plasticity component that uses a smoothed triaxial plastic yield surface developed from that used by Lubiner et al. (1989).

The crack plane model, that relates the local stresses to local strains, is a simplified version of a general crack plane model which uses contact mechanics to simulate crack closure with both shear and normal displacements, and thereby aggregate interlock (Jefferson, 2002a), and which uses multiple components to simulate the gradual transition of material fractions from a bonded undamaged state to a debonded damaged state during crack formation (Jefferson, 2002b).

2. Theoretical framework

2.1. Overall framework

The model employs plasticity, damage and contact theory in the formulation and thus has been classified p-d-c rather than the more commonly used classification of plastic-damage.

Definitions of the local and global stress and strain vectors, transformation relationships and elastic constitutive matrices are given in Appendix A. It is noted that the six-component vector form of Cartesian stress and strain tensors is used here.

A contact matrix ($\mathbf{M}_c$) is defined that has contributions from each POD. If no POD has formed then $\mathbf{M}_c$ is equal to the identity matrix.

The overall relationship between total stresses and strains is given by

$$\boldsymbol{\sigma} = \mathbf{M}_{\mathrm{c}}\mathbf{D}_{\mathrm{e}}(\boldsymbol{\varepsilon} - \boldsymbol{\varepsilon}_{\mathrm{p}}) \tag{1}$$

in which $\boldsymbol{\varepsilon}_{\mathrm{p}}$ is a plastic strain tensor.

The local stress–effective strain relationship, for a POD i, is given by

$$\mathbf{s}_i = \mathbf{D}_{\mathrm{ls}_i}\mathbf{e}_i \tag{2}$$

in which $\mathbf{D}_{\mathrm{ls}}$ is a local constitutive matrix, the form of which will be discussed in Section 3.

The local strains, $\mathbf{e}_i$, are the total effective local strains on a crack-plane. The added 'fracture' local strain vector is denoted $\mathbf{e}_{\mathrm{f}_i}$ and is related to the effective strain vector as follows

$$\mathbf{e}_{\mathrm{f}_i} = \mathbf{e}_i - \mathbf{C}_{\mathrm{L}}\mathbf{s}_i \tag{3}$$

$$\mathbf{e}_{\mathrm{f}_i} = \mathbf{C}_{\mathrm{lsf}_i}\mathbf{s}_i \tag{4}$$

where $\mathbf{C}_{\mathrm{lsf}}$ is a local compliance matrix.

It is emphasized that the primary crack plane variables used in these model computations are $\mathbf{e}$ and $\mathbf{s}$, and not $\mathbf{e}_{\mathrm{f}}$ and $\mathbf{s}$. This has the advantage that the model can be developed in terms of total local relative displacements (converted to strains), which means that experimental data can be used directly to develop governing functions.

Eq. (4) is used along with the stress transformation (A.1) to form the constitutive matrix as follows

$$\begin{aligned}\boldsymbol{\sigma} &= \mathbf{D}_{\mathrm{e}}(\boldsymbol{\varepsilon} - \boldsymbol{\varepsilon}_{\mathrm{p}} - \boldsymbol{\varepsilon}_{\mathrm{f}}) = \mathbf{D}_{\mathrm{e}}\left((\boldsymbol{\varepsilon} - \boldsymbol{\varepsilon}_{\mathrm{p}}) - \sum_{j=1}^{n_{\mathrm{p}}}\mathbf{N}_j^{\mathrm{T}}\mathbf{e}_{\mathrm{f}_j}\right) = \mathbf{D}_{\mathrm{e}}\left((\boldsymbol{\varepsilon} - \boldsymbol{\varepsilon}_{\mathrm{p}}) - \sum_{j=1}^{n_{\mathrm{p}}}\mathbf{N}_j^{\mathrm{T}}\mathbf{C}_{\mathrm{lsf}_j}\mathbf{s}_j\right)\\ &= \mathbf{D}_{\mathrm{e}}\left((\boldsymbol{\varepsilon} - \boldsymbol{\varepsilon}_{\mathrm{p}}) - \sum_{j=1}^{n_{\mathrm{p}}}\mathbf{N}_j^{\mathrm{T}}\mathbf{C}_{\mathrm{lsf}_j}\mathbf{N}_j\boldsymbol{\sigma}\right)\end{aligned} \tag{5}$$

and

$$\boldsymbol{\sigma} = \left(\mathbf{I} + \mathbf{D}_{\mathrm{e}}\sum_{j=1}^{n_{\mathrm{p}}}\mathbf{N}_j^{\mathrm{T}}\mathbf{C}_{\mathrm{lsf}_j}\mathbf{N}_j\right)^{-1}\mathbf{D}_{\mathrm{e}}(\boldsymbol{\varepsilon} - \boldsymbol{\varepsilon}_{\mathrm{p}}) = \mathbf{D}_{\mathrm{efc}}(\boldsymbol{\varepsilon} - \boldsymbol{\varepsilon}_{\mathrm{p}}) \tag{6}$$

in which $\mathbf{I}$ is the identity matrix and n_{p} is the number of PODs.

The strain tensor $(\boldsymbol{\varepsilon} - \boldsymbol{\varepsilon}_{\mathrm{p}} - \boldsymbol{\varepsilon}_{\mathrm{f}})$ will be referred to as the 'elastic' strain tensor and $(\boldsymbol{\varepsilon} - \boldsymbol{\varepsilon}_{\mathrm{p}})$ will be referred to as the 'recoverable' strain tensor.

The contact matrix is given by

$$\mathbf{M}_{\mathrm{c}} = \left(\mathbf{I} + \mathbf{D}_{\mathrm{e}}\sum_{j=1}^{n_{\mathrm{p}}}\mathbf{N}_j^{\mathrm{T}}\mathbf{C}_{\mathrm{lsf}_j}\mathbf{N}_j\right)^{-1} \tag{7}$$

Alternatively Eq. (6) may be written in terms of the compliance matrix as follows

$$(\boldsymbol{\varepsilon} - \boldsymbol{\varepsilon}_{\mathrm{p}}) = \mathbf{C}_{\mathrm{efc}}\boldsymbol{\sigma} \tag{8}$$

in which

$$\mathbf{C}_{\mathrm{efc}} = \left(\mathbf{C}_{\mathrm{e}} + \sum_{j=1}^{n_{\mathrm{p}}}\mathbf{N}_j^{\mathrm{T}}\mathbf{C}_{\mathrm{lsf}_j}\mathbf{N}_j\right)$$

2.2. Thermodynamic restrictions

The model should obey the first and second laws of thermodynamics and produce non-negative energy on any loading cycle. Considering mechanical energy alone, the second law may be expressed as (Meschke et al., 1998)

$$\boldsymbol{\sigma}^{\mathrm{T}}\dot{\boldsymbol{\varepsilon}} - \dot{\Psi}_{\mathrm{T}} \geqslant 0 \tag{9}$$

$\dot{\Psi}_{\mathrm{T}}$ is the Helmholtz free energy which here comprises two components, one the elastic recoverable strain energy $\dot{\Psi}$ and the other the latent, or locked in, energy $\dot{\Psi}_{\mathrm{L}}$ as follows

$$\dot{\Psi}_{\mathrm{T}} = \dot{\Psi} + \dot{\Psi}_{\mathrm{L}} \tag{10}$$

It will be assumed here that $\dot{\Psi}_{\mathrm{L}}$ is non-negative and is equal to a positive fraction of the total work rate minus the rate of change of stored elastic energy. Thus, to show that the model is dissipative, it is sufficient to prove that

$$\boldsymbol{\sigma}^{\mathrm{T}}\dot{\boldsymbol{\varepsilon}} - \dot{\Psi} \geqslant 0 \tag{11}$$

$$\psi = \tfrac{1}{2}(\boldsymbol{\varepsilon} - \boldsymbol{\varepsilon}_{\mathrm{p}})^{\mathrm{T}}\mathbf{D}_{\mathrm{efc}}(\boldsymbol{\varepsilon} - \boldsymbol{\varepsilon}_{\mathrm{p}}) = \tfrac{1}{2}\boldsymbol{\sigma}^{\mathrm{T}}\mathbf{C}_{\mathrm{efc}}\boldsymbol{\sigma} \tag{12}$$

It is noted that (12) applies to the case for which $\mathbf{C}_{\mathrm{efc}}$ simulates unloading to a stress free state in a linear manner.

Using (8) and (12) in (11) gives

$$\boldsymbol{\sigma}^{\mathrm{T}}[\dot{\mathbf{C}}_{\mathrm{efc}}\boldsymbol{\sigma} + \mathbf{C}_{\mathrm{efc}}\dot{\boldsymbol{\sigma}} + \dot{\boldsymbol{\varepsilon}}_{\mathrm{p}}] - \tfrac{1}{2}(\dot{\boldsymbol{\sigma}}^{\mathrm{T}}\mathbf{C}_{\mathrm{efc}}\boldsymbol{\sigma} + \boldsymbol{\sigma}^{\mathrm{T}}\dot{\mathbf{C}}_{\mathrm{efc}}\boldsymbol{\sigma} + \boldsymbol{\sigma}^{\mathrm{T}}\mathbf{C}_{\mathrm{efc}}\dot{\boldsymbol{\sigma}}) \geqslant 0 \tag{13}$$

If the part associated with plastic straining is separated from the rest of the equation, then (13) is satisfied if

$$\boldsymbol{\sigma}^{\mathrm{T}}\dot{\boldsymbol{\varepsilon}}_{\mathrm{p}} \geqslant 0 \tag{14a}$$

and

$$\boldsymbol{\sigma}^{\mathrm{T}}\dot{\mathbf{C}}_{\mathrm{efc}}\boldsymbol{\sigma} + \boldsymbol{\sigma}^{\mathrm{T}}(\mathbf{C}_{\mathrm{efc}} - \mathbf{C}_{\mathrm{efc}}^{\mathrm{T}})\dot{\boldsymbol{\sigma}} \geqslant 0 \tag{14b}$$

By using (8) in (14b) and applying the transformation (A.1) it may be shown that (14b) is satisfied if the local form is satisfied for all PODs i as follows

$$\mathbf{s}_i^{\mathrm{T}}\dot{\mathbf{C}}_{\mathrm{lsf}_i}\mathbf{s}_i + \mathbf{s}_i^{\mathrm{T}}(\mathbf{C}_{\mathrm{lsf}_i} - \mathbf{C}_{\mathrm{lsf}_i}^{\mathrm{T}})\dot{\mathbf{s}}_i \geqslant 0 \tag{15}$$

The conditions (14a) and (15) are those required for ensuring that the model always predicts non-negative dissipation on a closed loading cycle. The conditions have been derived allowing for the possibility that both $\mathbf{C}_{\mathrm{efc}}$ and $\mathbf{C}_{\mathrm{lsf}}$ are asymmetric.

3. Model components

3.1. Local damage-contact relationships

The essential idea of the fracture part of the model is to use the stress–strain relationship of an effective crack plane to generate a relationship between added local fracture strains and local stresses.

The local stress–effective strain model employs a simplified version of the effective crack plane model developed by the author (Jefferson, 2002b), but here only the damage and contact components are used. It is noted that here local strains rather than relative-displacements are used, but that the strain parameters

depend upon a characteristic length and the fracture energy per unit area following the approach of Bazant and Oh (1983). In finite element applications this characteristic length is dependent on the element size (Bazant and Oh, 1983; Oliver, 1990).

In the crack plane model it is assumed that a representative volume comprises two components of material: (i) undamaged material and (ii) fully-debonded material. The proportions of material in each component, per unit representative area, are denoted h_c and h_f respectively and h_c and h_f must satisfy the following conditions

$$h_c + h_f = 1, \quad 0 \leqslant h_c \leqslant 1, \;\; 0 \leqslant h_f \leqslant 1 \tag{16}$$

If the h terms are compared with those used in an isotropic damage model, in which the scalar damage variable is ω, then $h_c = 1 - \omega$. h_c is a function of a scalar damage variable ζ, and h_f depends upon the contact condition and the state of damage. The local stress is the sum of the stresses on the two components as follows

$$\mathbf{s} = h_c(\zeta)\mathbf{D}_L\mathbf{e} + h_f(\zeta, \mathbf{e})\mathbf{s}_f \tag{17}$$

in which $\mathbf{s}_f$ is the local stress vector for the fully-debonded material component.

Following Jefferson (2002a), three states of contact are defined for a crack plane that are termed open, interlock and closed. These are illustrated in Fig. 1 in local strain space.

Experimental evidence suggests that once a crack has opened on a plane, contact can be regained with shear, as well as normal, movement and that the contact surface can be reasonably simulated with a linear function in strain space (Jefferson, 2002a), as shown in Fig. 1.

In the open state the stress in the debonded component is assumed zero. In the interlock state the debonded stress is derived from a contact law in which the stress is assumed to depend upon the distance (in local strain terms) to the contact surface that is denoted by the vector $\mathbf{g}$ and which is termed the embed-

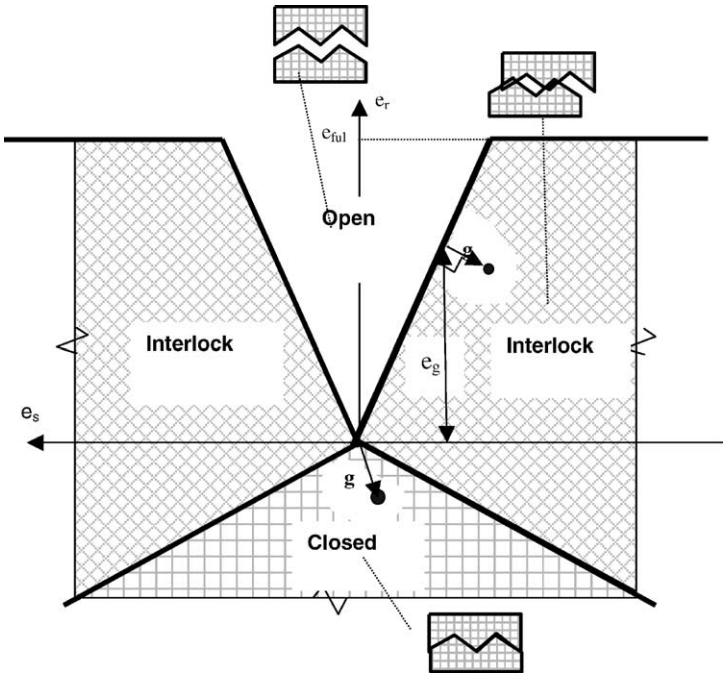

Fig. 1. Local contact states.

ment. In the closed state, **g** is equal to the local strain vector since the contact point coincides with the origin of the local strain space.

The interlock and closed functions used to identify which state is active are

$$\phi_{\text{int}}(\mathbf{e}) = m_g e_{\text{r}} - \sqrt{e_{\text{s}}^2 + e_{\text{t}}^2} \tag{18a}$$

$$\phi_{\text{cl}}(\mathbf{e}) = e_{\text{r}} + m_g \sqrt{e_{\text{s}}^2 + e_{\text{t}}^2} \tag{18b}$$

If $\phi_{\text{cl}}(\mathbf{e}) \leqslant 0$ State = Closed
If $\phi_{\text{cl}}(\mathbf{e}) > 0$ and $\phi_{\text{int}}(\mathbf{e}) < 0$ and $e_{\text{r}} < e_{\text{ful}}$ State = Interlock
If $\phi_{\text{int}}(\mathbf{e}) \geqslant 0$ or $e_{\text{r}} \geqslant e_{\text{ful}}$ State = Open

The constant m_g can be obtained from experimental data from tests in which shear is applied to an open crack, for example from the tests conducted by Walraven and Reinhardt (1981). In Jefferson (2002a) m_g was taken as a constant of value 0.3 but from the data presented in that reference it is considered that a reasonable range for m_g for normal strength concrete is 0.3–0.6. It was found that a low value of 0.3 could lead to second cracks forming at shallow angles to the first, due to the development of relatively large shear forces, and therefore a larger value of 0.5 is recommended as the default.

In the interlock state the direction of **g** is fixed by the normal to the interlock function and therefore the embedment can be expressed in terms of the positive scalar g (always positive in the interlock state) and the normal as follows

$$\mathbf{g} = \left(-\frac{\partial \phi_{\text{int}}}{\partial \mathbf{e}} \Big/ \left| \frac{\partial \phi_{\text{int}}}{\partial \mathbf{e}} \right| \right) g = \mathbf{n}_i g \tag{19}$$

The embedment may also be obtained from a transformation of the local strains as follows

$$\mathbf{g} = \mathbf{\Phi}_g \mathbf{e} \tag{20}$$

where

$$\mathbf{\Phi}_g = \frac{1}{1 + m_g^2} \left(\left(\frac{\partial \phi_{\text{int}}}{\partial \mathbf{e}} \right) \left(\frac{\partial \phi_{\text{int}}}{\partial \mathbf{e}} \right)^{\text{T}} + \phi_{\text{int}} \frac{\partial^2 \phi_{\text{int}}}{\partial \mathbf{e}^2} \right) \tag{21}$$

There is a crack opening strain beyond which no further contact can be gained in shear and this is denoted e_{ful}. In this implementation of the model, e_{ful} is made a multiple of ε_0, i.e. $e_{\text{ful}} = m_{\text{ful}} \varepsilon_0$. Trials suggest that when concrete contains relatively large coarse aggregate i.e. 20–30 mm, a value of m_{ful} in the range 10–20 is appropriate, whereas for concrete with relatively small coarse aggregate, i.e. 5–8 mm, a lower value is appropriate, in the range 3–5. This variation is necessary because the relative displacement at the end of a tension-softening curve (related via the characteristic dimension to ε_0) is not in direct proportion to the coarse aggregate size, whereas, as was shown in Jefferson (2002a,b), the clearance displacement is roughly in proportion to the coarse aggregate size. Thus e_{ful} is not in a fixed ratio to ε_0.

As a crack opens the relative proportion of debonded material that can regain contact in shear reduces as crack opening increases. Walraven and Reinhardt (1981) developed two linear functions that relate normal and shear displacements to the associated stresses. A function for h_{f} that, when applied in Eq. (17), fits these linear relationships with reasonable accuracy is given below

$$
\begin{aligned}
h_{\mathrm{f}} &= (1 - h_{\mathrm{c}})H_{\mathrm{f}} \\
H_{\mathrm{f}} &= H_{\mathrm{m}} \quad \text{if } e_{\mathrm{r}} < \varepsilon_{\mathrm{t}} \\
H_{\mathrm{f}} &= H_{\mathrm{m}} \left\{ r_{\mathrm{f}} e^{-\rho_{\mathrm{f}_1}\left(\frac{e_g - \varepsilon_{\mathrm{t}}}{\varepsilon_0}\right)^2} + (1 - r_{\mathrm{f}}) e^{-\rho_{\mathrm{f}_2}\left(\frac{e_g - \varepsilon_{\mathrm{t}}}{\varepsilon_{\mathrm{ful}}}\right)^2} \right\} \left(1 - e^{-c_g \frac{g}{e_g + 2\varepsilon_{\mathrm{t}}}}\right)
\end{aligned}
\tag{22}
$$

where $r_{\mathrm{f}} = 0.95$, $\rho_{\mathrm{f}_1} = 4$, $\rho_{\mathrm{f}_2} = 1.5$, $c_g = 3$, ε_{t} is uniaxial strain at first fracture and ε_0 is the strain at the effective end of the softening curve, as illustrated in Fig. 2. H_{m} is set to 0.995 rather than 1 for reasons explained in Section 6, which discusses the thermodynamics of the model.

H_{f} may be thought of as representing the proportion of the damaged material on a POD that is in contact. The function is smooth with respect to the opening displacement e_g and also provides a smooth, though rapid, transition to Closed and Interlock states, via the last term in Eq. (22). The latter term can, however, be set to unity for single point constitutive simulations. The purpose of using smooth functions is to improve the convergence properties of the model when implemented with Newton iterative solution algorithms.

Here, the variable e_g, which is defined in Fig. 1, is used to measure the opening displacement rather than component e_{r}. The advantage of using e_g is that unloading along $\mathbf{g}$ to the surface is linear and thus the free energy associated with interlock contact takes a familiar quadratic form. e_g is related to the components of the effective local strain, as follows

$$
e_g = \frac{1}{1 + m_g^2}\left[e_1 + m_g\sqrt{e_2^2 + e_3^2}\right] \tag{23}
$$

In direct tension the damage model should produce the type of characteristic softening curve shown in Fig. 2. When the material has experienced a degree of 'crushing' in compression there is a general loss of tensile strength (Kupfer et al., 1969), and in the present model this is simulated with an increase in damage and a reduction in the first fracture stress. It is recognized that apparent 'crushing' in, for example, a concrete cube test largely involves diffuse cracking and therefore its simulation with increased damage is considered reasonable.

$$
h_{\mathrm{c}} = r_{\mathrm{c}}\frac{\varepsilon_{\mathrm{t}}}{\zeta} + \left[(1 - r_{\mathrm{c}})\frac{\varepsilon_{\mathrm{t}}}{\zeta} e^{-c_2\frac{\zeta - \varepsilon_{\mathrm{t}}}{\varepsilon_0 - \varepsilon_{\mathrm{t}}}}\right] e^{-2\frac{\kappa}{\kappa_{\mathrm{p}}}} \tag{24}
$$

where the first fracture strain $\varepsilon_{\mathrm{t}} = f_{\mathrm{t}}/E$, f_{t} is the tensile strength and E the Young modulus.

The terms κ and κ_{p} are the plastic parameter and peak plastic parameter values, respectively. These are explained in context, in Section 3.2. The constant c_2 is set to a fixed value of 5.

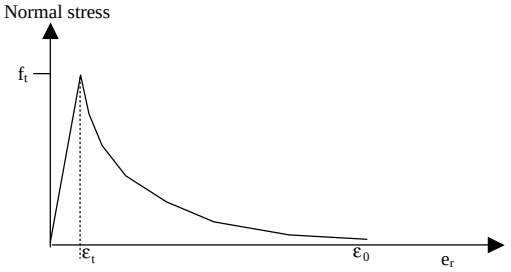

Fig. 2. Characteristic tensile softening curve.

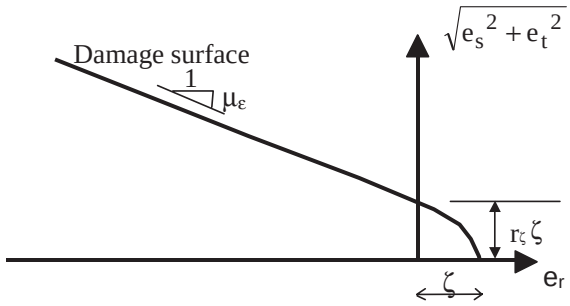

Fig. 3. Local damage surface.

In Eq. (24) the damage strain parameter ζ is set to an initial value of ε_t. The first term in (24) serves to provide residual damage strength that is useful for stabilizing numerical calculations and maintaining a residual damage stress. r_c was set to 0.01 for the constitutive simulations in the present paper.

A POD is assumed to form when the principal stress reaches the fracture stress (f_t), with the POD being normal to the major principal axis. Thereafter, it is assumed that damage on the plane can occur with both shear and normal strains. The damage surface, which is similar to that used by Kroplin and Weihe (1997) and is illustrated in Fig. 3, is as follows

$$\phi(\mathbf{e},\zeta) = \frac{e_r}{2}\left[1 + \left(\frac{\mu_\varepsilon}{r_\zeta}\right)^2\right] + \frac{1}{2r_\zeta^2}\sqrt{\left(r_\zeta^2 - \mu_\varepsilon^2\right)^2 e_r^2 + 4r_\zeta^2\left(e_s^2 + e_t^2\right)} - \varsigma \tag{25}$$

The material constants r_ζ and μ_ε are the strain equivalents of the relative shear stress intercept $r_\sigma = c/f_t$ and the asymptotic friction factor μ, noting that c is the shear stress intercept. These, the stress ratios, are set to 0.8 and 0.5 respectively.

The constitutive relationship for the effective crack plane can now be written

$$\mathbf{s} = \mathbf{D}_L(h_c\mathbf{e} + h_f\mathbf{g}) = \mathbf{D}_L(h_c\mathbf{I} + h_f\boldsymbol{\Phi}_d)\mathbf{e} = \mathbf{D}_{ls}\mathbf{e} = \mathbf{D}_L\mathbf{M}_x\mathbf{e} \tag{26}$$

where

$$\boldsymbol{\Phi}_d = \mathbf{0} \quad \text{if State} = \text{Open}$$
$$\boldsymbol{\Phi}_d = \boldsymbol{\Phi}_g \quad \text{if State} = \text{Interlock}$$
$$\boldsymbol{\Phi}_d = \mathbf{I} \quad \text{if State} = \text{Closed}$$

Using Eqs. (3) and (4), the relationship between the stress and added fracture strain can be derived to be

$$\mathbf{e}_f = (\mathbf{M}_x^{-1} - \mathbf{I})\mathbf{C}_L\mathbf{s} = \mathbf{C}_{lsf}\mathbf{s} \tag{27}$$

Alternatively, the added fracture strains may be expressed in terms of the effective local strains as follows

$$\mathbf{e}_f = (\mathbf{I} - \mathbf{M}_x)\mathbf{e} \tag{28}$$

3.2. Plasticity component

3.2.1. Triaxial behavior

Experiments on concrete in compression show a number of characteristic features (Kotsovos and Newman, 1979), which include;

- significant non-linearity up to a peak stress with post-peak softening thereafter,
- increased deviatoric strength with triaxial confinement,
- unloading–reloading behavior that is near elastic until well into the post-peak range, except under high confining pressures.

A relatively simple, but powerful, plasticity component is included in the present model. A smooth triaxial yield surface is developed from the yield function used by Lubiner et al. (1989) and from Willam and Warnke's (1975) smoothing function. Since a consistent formulation is to be used in the final implementation, the second derivative of the yield function is required, and therefore it was considered expedient to use a relatively simple yield surface with straight meridians.

The model includes friction hardening and softening to account for pre and post peak non-linear behavior, and uses work hardening in which the total work required to reach the peak stress envelope is made a function of the mean stress. The model is developed with a dilatancy parameter that allows plastic flows to be associated or non-associated, although to simulate experiments accurately non-associated flow is required.

The accuracy of the model reduces for stress states with high triaxial confinement because the model does not simulate non-linearity under hydrostatic compression and the yield function has straight meridians. This is quantified in Section 7, where a confining limit is suggested beyond which the model is considered inaccurate.

3.2.2. Yield function

The yield function adopts the same meridians, in octahedral stress space, as those used in the compressive part of the model of Lubiner et al. (1989), however, to avoid having discontinuities in the pi-plane, as in the Lubliner surface, the smoothing function of Willam and Warnke (1975) is employed. This smoothing function simplifies considerably if the eccentricity parameter (ρ) is set to a constant value of $1/\sqrt{2}$. The resulting function is as follows

$$F(\boldsymbol{\sigma}, Z(\kappa)) = \sqrt{J_2} A_r(\theta) + \left(\alpha + \frac{\gamma}{3}\right) I_1 Z - f_c Z(1-\alpha) \tag{29}$$

where

$$A_r(\theta) = \rho_c \left(\frac{2\cos(\theta)^2 + b^2}{\cos(\theta) + b\sqrt{2\cos(\theta)^2 + c}} \right)$$

and I_1 is the first stress invariant, J_2, the second deviatoric stress invariant, θ is the Lode angle (with range 0–60°) and Z is a friction hardening factor, which is a function of the work hardening parameter κ. Z varies from a possible value of 0, at which the yield surface degenerates to a line on the hydrostatic axis, up to 1 at the peak surface position. The initial position of the yield surface is governed by the initial value of $Z = Z_0$. For most situations in which the degree of triaxial confinement is relatively low, a value of between 0.5 and 0.6 is considered appropriate for Z_0 however, for higher confinements a lower value of 0.25 is better. The boundaries between 'low and high confinements are discussed under Example 5 in Section 7.

The material parameters required to define the constants are the uniaxial compressive strength f_c and the ratio between the biaxial and uniaxial strengths b_r, which is generally in the range 1.05–1.3 (Kupfer et al., 1969; van Mier, 1997). The constants in Eq. (29) are then obtained, in the manner described by Lubiner et al. (1989), using the following expressions

$$\alpha = \frac{b_r - 1}{2b_r - 1}, \quad b = \sqrt{2} - 1, \quad c = \frac{5}{2} - 2\sqrt{2}, \quad \rho = 1/\sqrt{2}, \quad \gamma = \frac{3(1-\rho)}{2\rho - 1}, \quad \rho_c = \sqrt{3} + \frac{\gamma}{\sqrt{3}}$$

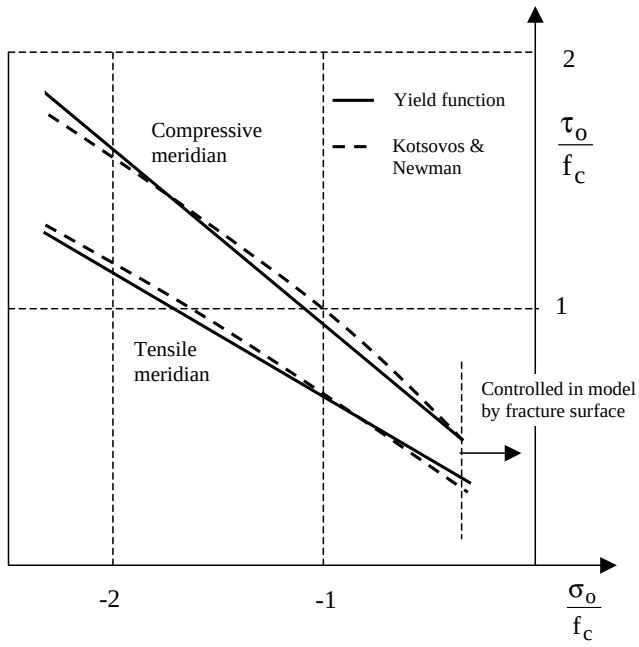

Fig. 4. Yield function meridians.

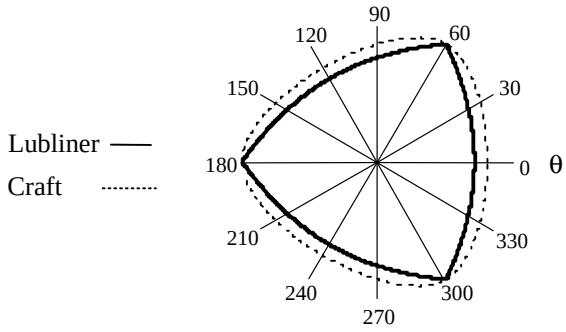

Fig. 5. Yield function on the pi-plane.

A comparison between the experimentally determined curves of Kotsovos and Newman (1979) and the meridians from the yield surface is shown in Fig. 4. A comparison with the surface of Lubiner et al. (1989) in the pi-plane is shown in Fig. 5.

3.2.3. Plastic potential and flow rule

The plastic potential function, given below, is obtained directly from (29) but an additional parameter (ψ) is added which can be used to control the degree of dilatancy. Associated flow is achieved if $\psi = 1$, but it was found that ψ values in the range -0.1 to -0.3 were required to match experimental data. Generally ψ is set to -0.1, but for high degrees of triaxial confinement -0.3 provides a better match to experimental data.

$$G(\boldsymbol{\sigma}, Z(\kappa)) = \sqrt{J_2}A_r(\theta) + \left(\alpha + \frac{\gamma}{3}\right)I_1 Z\psi - f_c Z\psi(1-\alpha) \tag{30}$$

The flow rule is derived from the plastic potential in the standard way as follows

$$\dot{\boldsymbol{\varepsilon}}_p = \frac{\partial G}{\partial \boldsymbol{\sigma}}\dot{\lambda} \tag{31}$$

λ is the plastic multiplier, which obeys the condition $\dot{\lambda} \geqslant 0$.

The restriction on ψ, supplied by expression (14a), may be expressed as

$$\boldsymbol{\sigma}^T \frac{\partial G}{\partial \boldsymbol{\sigma}} \geqslant 0 \tag{32}$$

and is satisfied if $\psi \geqslant -1$.

3.2.4. Hardening/softening relationships

A work hardening hypothesis is made for the present model, and it is assumed that the amount of work to achieve peak stress increases with the mean stress, according to a parameter X. This parameter performs essentially the same role as the ductility parameter of Este and Willam (1994). The work hardening parameter, expressed in rate form, is given by

$$\dot{\kappa} = X(\boldsymbol{\sigma})\boldsymbol{\sigma}^T\dot{\boldsymbol{\varepsilon}}_p \tag{33}$$

A single friction hardening/softening function for Z has been adopted which gives a smooth transition from pre- to post-peak behavior, as follows

$$Z = Z_0 + \frac{(1-Z_0)}{a_c}e^{-c_{c1}\eta}(1 - e^{-c_{c2}\eta}) \tag{34}$$

where $\eta = \kappa/\kappa_p$, κ_p, the value of κ at the peak yield surface position; and to ensure that the peak occurs at $Z = 1$, the constants of (34) must satisfy the following relationships $c_{c1} = \frac{c_{c2}e^{-c_{c2}}}{1-e^{-c_{c2}}}$ and $a_c = e^{-c_{c1}}(1 - e^{-c_{c2}})$. The actual values used are $c_{c2} = 5$, $c_{c1} = 0.0339182745$ and $a_c = 0.9601372615$.

The following expression for κ_p was derived by integrating Saenz's (1964) equation over a uniaxial stress–strain curve in compression and then removing the elastic component, using data typical for structural concrete

$$\kappa_p = f_c\left(0.72\varepsilon_c - \frac{f_c}{2E}\right) \tag{35}$$

in which ε_c is the uniaxial compressive strain at the peak uniaxial compressive stress (f_c).

The expression used for the enhancement factor is as follows

$$X = e^{\chi} + e^{\chi-1} + X_I \tag{36}$$

where $\chi = I_1/(f_c \times 0.9) + 0.55$ and $X_I = 0.0022$ it should remembered that the enhancement factor will never be required for stress states for which I_1 is positive i.e. tensile.

4. Constitutive matrix and stress update computations

For the finite element implementation of the model, a consistent algorithm was developed for the tangent matrix and stress recovery computations following the principles established for computational plasticity by Simo and Taylor (1985), but extending the approach to the present p-d-c model. This algorithm is described in a linked publication Jefferson (2003), but here the more standard form of the tangent con-

stitutive matrix and stress recovery algorithms are described, which were employed for much of the work on the single point stress/strain path simulations.

4.1. Tangent constitutive matrix

The stress–strain rate relationship may be written as follows, if any variation in $\mathbf{N}_i$ is ignored.

$$\dot{\boldsymbol{\sigma}} = \mathbf{D}_{\mathrm{e}}\left((\dot{\boldsymbol{\varepsilon}} - \dot{\boldsymbol{\varepsilon}}_{\mathrm{p}}) - \sum_{j=1}^{n_{\mathrm{p}}} \mathbf{N}_j^{\mathrm{T}} \dot{\mathbf{e}}_{\mathrm{f}}\right) \tag{37}$$

The local stress–strain rate relationship for each POD is considered as follows, noting that here the POD subscript is temporarily dropped for clarity.

$$\dot{\mathbf{s}} = \mathbf{D}_{\mathrm{L}}\left[\left(\mathbf{M}_x + \frac{\partial \mathbf{M}_x}{\partial \mathbf{e}}\mathbf{e}\right)\dot{\mathbf{e}} + \frac{\partial \mathbf{M}_x}{\partial \kappa}\mathbf{e}\dot{\kappa}\right] = \mathbf{D}_{\mathrm{L}}\left(\mathbf{M}'_x\dot{\mathbf{e}} + \mathbf{m}'_\kappa\dot{\kappa}\right) \tag{38}$$

$$\dot{\mathbf{e}} = \mathbf{M}'^{-1}_x[\mathbf{C}_{\mathrm{L}}\dot{\mathbf{s}} - \mathbf{m}'_\kappa\dot{\kappa}] \tag{39}$$

$$\dot{\mathbf{e}}_{\mathrm{f}} = (\mathbf{M}'^{-1}_x - \mathbf{I})\mathbf{C}_{\mathrm{L}}\dot{\mathbf{s}} - \mathbf{M}'^{-1}_x\mathbf{m}'_\kappa\dot{\kappa} = \mathbf{C}_{\mathrm{ltf}}\dot{\mathbf{s}} - \boldsymbol{\varpi}_\kappa\dot{\kappa} \tag{40}$$

where

$$\mathbf{M}'_x = \mathbf{M}_x + \frac{\partial \mathbf{M}_x}{\partial \mathbf{e}} \circ \mathbf{e}$$

$$\boldsymbol{\varpi}_\kappa = \mathbf{M}'^{-1}_x\mathbf{m}'_\kappa$$

$$\frac{\partial \mathbf{M}_x}{\partial \mathbf{e}} \circ \mathbf{e} = \left(\frac{\mathrm{d}h_{\mathrm{c}}}{\mathrm{d}\zeta}\mathbf{e}\frac{\partial \zeta^{\mathrm{T}}}{\partial \mathbf{e}} + \left(\frac{\mathrm{d}h_{\mathrm{f}}}{\mathrm{d}\zeta}\mathbf{e}\frac{\partial \zeta^{\mathrm{T}}}{\partial \mathbf{e}} + \frac{\mathrm{d}h_{\mathrm{f}}}{\mathrm{d}e_g}\mathbf{e}\frac{\partial e_g^{\mathrm{T}}}{\partial \mathbf{e}} + \frac{\mathrm{d}h_{\mathrm{f}}}{\mathrm{d}g}\mathbf{e}\frac{\partial g^{\mathrm{T}}}{\partial \mathbf{e}}\right)\boldsymbol{\Phi}_{\mathrm{d}}\right)$$

$$\mathbf{m}'_\kappa = \frac{\partial h_{\mathrm{c}}}{\partial \kappa}\mathbf{e} + \frac{\partial h_{\mathrm{f}}}{\partial \kappa}\boldsymbol{\Phi}_{\mathrm{d}}\mathbf{e}$$

in which $\circ$ denotes a general matrix vector contraction.

The relationship between the local and global stress rates is as follows

$$\dot{\mathbf{s}}_i = \mathbf{N}_i\dot{\boldsymbol{\sigma}} \tag{41}$$

It is noted that in the consistent algorithm the rate of $\mathbf{N}_i$ is also included, which is only non-zero within the increment a POD first forms.

Substituting for $\dot{\boldsymbol{\varepsilon}}_{\mathrm{p}}$ and $\dot{\mathbf{e}}_{\mathrm{f}}$ in Eq. (37), using (31) and (40) respectively gives

$$\dot{\boldsymbol{\sigma}} = \mathbf{D}_{\mathrm{e}}\left(\left(\dot{\boldsymbol{\varepsilon}} - \frac{\partial G}{\partial \boldsymbol{\sigma}}\dot{\lambda}\right) - \sum_{j=1}^{n_{\mathrm{p}}} \mathbf{N}_j^{\mathrm{T}}(\mathbf{C}_{\mathrm{ltf}}\dot{\mathbf{s}} - \boldsymbol{\varpi}_\kappa\dot{\kappa})\right) \tag{42}$$

Substituting for $\dot{\kappa}$ from (33), for $\dot{\mathbf{s}}$ from (38) and rearranging gives

$$\dot{\boldsymbol{\sigma}} = \mathbf{D}_{\mathrm{tefc}}(\dot{\boldsymbol{\varepsilon}} - \mathbf{g}_{\mathrm{m}}\dot{\lambda}) \tag{43}$$

in which

$$\mathbf{D}_{\text{tefc}} = \left(\mathbf{I} + \mathbf{D}_{\text{e}} \sum_{i=1}^{n_{\text{p}}} \mathbf{N}_i^{\text{T}} \mathbf{C}_{\text{ltf}_i} \mathbf{N}_i \right)^{-1} \mathbf{D}_{\text{e}}$$

$$\mathbf{g}_{\text{m}} = \frac{\partial G}{\partial \boldsymbol{\sigma}} - \sum_{j=1}^{n} \mathbf{N}_j^{\text{T}} \boldsymbol{\varpi}_{\kappa} X \boldsymbol{\sigma}^{\text{T}} \frac{\partial G}{\partial \boldsymbol{\sigma}}$$

Applying the consistency condition to the yield surface gives

$$\frac{\partial F^{\text{T}}}{\partial \boldsymbol{\sigma}} \dot{\boldsymbol{\sigma}} + \frac{\delta F}{\delta \kappa} \dot{\kappa} = 0 \tag{44}$$

substituting for $\dot{\boldsymbol{\sigma}}$ from (43) and $\dot{\kappa}$ from (33) and rearranging gives

$$\dot{\lambda} = \frac{\left(\frac{\partial F}{\partial \boldsymbol{\sigma}}\right)^{\text{T}} \mathbf{D}_{\text{tefc}}}{\left(\frac{\partial F}{\partial \boldsymbol{\sigma}}\right)^{\text{T}} \mathbf{D}_{\text{efc}} \mathbf{g}_{\text{m}} - h_{\kappa}} \dot{\boldsymbol{\varepsilon}} \tag{45}$$

in which $h_{\kappa} = \frac{\partial F}{\partial \kappa} X \boldsymbol{\sigma}^{\text{T}} \frac{\partial G}{\partial \boldsymbol{\sigma}}$.

Using (45) in (43) gives the tangent elasto-plastic-damage-contact matrix

$$\dot{\boldsymbol{\sigma}} = \left(\mathbf{D}_{\text{tefc}} - \frac{\mathbf{D}_{\text{tefc}} \frac{\partial G}{\partial \boldsymbol{\sigma}} \left(\frac{\partial F}{\partial \boldsymbol{\sigma}}\right)^{\text{T}} \mathbf{D}_{\text{tefc}}}{\left(\frac{\partial F}{\partial \boldsymbol{\sigma}}\right)^{\text{T}} \mathbf{D}_{\text{efc}} \mathbf{g}_{\text{m}} - h_{\kappa}} \right) \dot{\boldsymbol{\varepsilon}} \tag{46}$$

4.2. Stress recovery

4.2.1. Overall approach

The approach adopted in this stress recovery algorithm is first to update the effective local strains and then account for any plastic flow, with the later computation employing the updated e-f-c constitutive matrix. The plasticity equations are then satisfied using a Tangent Cutting algorithm (Ortiz and Simo, 1986).

4.2.2. Local strain update

It is important that the governing relationships between global strains and stresses (Eq. (1)); local and global stresses (Eq. (A.1)); local stresses and effective local strains (Eq. (26)) and local effective strains, added fracture strains and local stresses (Eq. (3)) are all satisfied in the stress computations. Using these equations, a set of coupled equations may be derived in which the unknowns are the effective local fracture strains of each POD ($\mathbf{e}_i$) as follows

$$\mathbf{f}_{\text{e}_i} = \mathbf{N}_i \left[\mathbf{D}_{\text{e}} \left(\boldsymbol{\varepsilon}^k - \boldsymbol{\varepsilon}_{\text{p}}^{k-1} \right) - \sum_{j=1}^{n_{\text{p}}} \mathbf{N}_j^{\text{T}} \left(\mathbf{I} - \mathbf{M}_{x_j} \right) \mathbf{e}_j^k \right] - \mathbf{D}_{\text{ls}_i} \mathbf{e}^k = \mathbf{0} \tag{47}$$

The superscript k denotes the iteration number and update is from the last iteration, which is in contrast to the more rigorous consistent FE version of the algorithm in which all updates are made from last converged state. These non-linear equations are solved using a Newton–Raphson approach. Typically one to two iterations are required for a case with a single POD, three iterations for two PODs and five iterations for three PODs. The name total–local function is introduced for Eq. (47) because it maintains, simultaneously, the local and total constitutive governing relationships. Once any new PODs have been formed and the local strains updated using Eq. (47), the secant elastic-damage-contact matrix ($\mathbf{D}_{\text{efc}}$) is formed and the trial stresses computed for the plasticity stress reduction phase.

A restriction which the author has chosen to place on (47) is that relationship between the effective local strains ($\mathbf{e}_i$) and the total 'elastic' strain tensor ($\boldsymbol{\varepsilon} - \boldsymbol{\varepsilon}_p$) should always be unique. This places some restrictions on the form of the local stiffness matrix that will be discussed in Section 5.

4.2.3. Update algorithm

The trial stress is first computed from Eq. (48), the yield function is then checked and if the yield function value exceeds zero, Eqs. (49)–(51) are applied sequentially until the yield function converges to within a given tolerance of zero, at which point the global stress $\boldsymbol{\sigma}$ is updated to the value $\boldsymbol{\sigma}_{tr}$.

$$\boldsymbol{\sigma}_{tr} = \mathbf{D}^k_{efc}(\boldsymbol{\varepsilon}^k - \boldsymbol{\varepsilon}^{k-1}_p) \tag{48}$$

$$\Delta\lambda = \frac{F(\boldsymbol{\sigma}_{tr}, Z(\kappa))}{\left(\frac{\partial F}{\partial \boldsymbol{\sigma}}\right)^T \mathbf{D}_{efc} \frac{\partial G}{\partial \boldsymbol{\sigma}} - h_\kappa(\kappa)} \tag{49}$$

$$\boldsymbol{\sigma}_{tr} = \boldsymbol{\sigma}_{tr} - \frac{\partial G}{\partial \boldsymbol{\sigma}} \Delta\lambda \tag{50}$$

$$\Delta\kappa = X(\boldsymbol{\sigma}_{tr}) \boldsymbol{\sigma}^T_{tr} \frac{\partial G}{\partial \boldsymbol{\sigma}} \Delta\lambda : \quad \kappa = \kappa + \Delta\kappa \tag{51}$$

in which Δ denotes the change in a variable and superscript k denotes the overall iteration number.

It is noted that the value of κ used in the evaluation of $\mathbf{D}_{efc}$ is that from the last iteration, and since this secant form has accounted for changes in κ, it is appropriate here to use $\partial G/\partial \boldsymbol{\sigma}$, rather than $\mathbf{g}_m$, in the denominator of Eq. (49).

It is emphasized that this algorithm is only suitable for relatively small steps, as may be used in simulations with a constitutive driver, but the use of this stress update with the tangent matrix given in (46) would be unwise in a finite element implementation, in which strain step sizes can be much larger.

5. Implications of different forms of local elastic constitutive matrix

A general form of the local elastic constitutive matrix is given below in Eq. (52).

$$\mathbf{D}_L = \begin{bmatrix} E_n & 0 & 0 \\ 0 & E_\tau & 0 \\ 0 & 0 & E_\tau \end{bmatrix} \tag{52}$$

A number of options for the values of E_n and E_τ were considered during the development of the model. The first, which is perhaps the natural choice, is that $E_n = E$ (Young's modulus) and $E_\tau = G$ (the elastic shear modulus), such that the relationship between local stresses and effective local strains is based on the uniaxial elastic and shear moduli. Noting that $G = E/2(1+\upsilon)$.

A second option is based on the observation that $\mathbf{D}_L = \mathbf{N}_i \mathbf{D}_e \mathbf{N}^T_j$ for $i = j$, if $E_n = E_{ef}$ and $E_\tau = G$. With this form of $\mathbf{D}_L$ Eq. (47) reduces to

$$\mathbf{N}_l \mathbf{D}_{el}(\boldsymbol{\varepsilon} - \boldsymbol{\varepsilon}_p) = \mathbf{D}_L \mathbf{e}_l \tag{53}$$

$$E_{ef} = E\frac{1-\upsilon}{(1+\upsilon)(1-2\upsilon)} \text{ for 3D, plane strain and axisymmeric cases}$$

$$E_{ef} = E\frac{1}{(1-\upsilon^2)} \text{ for the plane stress case}$$

This means that for the one POD case there is a direct relationship between the local effective strains and the recoverable strains ($\boldsymbol{\varepsilon} - \boldsymbol{\varepsilon}_{\mathrm{p}}$).

A third option was considered because the thermodynamic restriction summarized in inequality (15) simplifies to the more manageable form shown in Eq. (54) if $\mathbf{C}_{\mathrm{lsf}}$ is symmetric. The forms considered in options one and two both result in $\mathbf{C}_{\mathrm{lsf}}$ being non-symmetric in the interlock state, however if $E_n = E_\tau$ then both $\mathbf{D}_{\mathrm{ls}}$ and $\mathbf{C}_{\mathrm{lsf}}$ are always symmetric since $\boldsymbol{\Phi}_{\mathrm{d}}$ is always symmetric.

$$\mathbf{s}_i^{\mathrm{T}} \dot{\mathbf{C}}_{\mathrm{lsf}_i} \mathbf{s}_i \geqslant 0 \tag{54}$$

Options one and two are similar with E_τ being the same for both options and E_{ef} being typically within 10% of E. Since option two leads to a simplification of Eq. (47) only option two will be discussed further.

The thermodynamic assessment of the model will be made for both the symmetric and the asymmetric forms of $\mathbf{C}_{\mathrm{lsf}}$ and it is noted that both options were implemented. However for option two, the ratio between the normal and shear stiffness is consistent with the properties of a band of elastic material, which suggests that data from shear-normal tests can be used directly to calibrate the model. Furthermore, option two proved to provide better fits to experimental data, as may be seen in Example 3 of Section 7, than option three. Therefore option two was the one chosen for the finite element simulations in the associated paper. The decision to use option two is however tentative because it did not prove possible to derive a formal proof that the model with this asymmetric form of $\mathbf{C}_{\mathrm{lsf}}$ satisfied the second law of thermodynamics for all cases, whereas such a proof was possible for the symmetric case, at least for 2D problems.

6. Thermodynamic assessment

6.1. Plasticity component

The general thermodynamic restrictions were summarized in expressions (14a) and (15). Dealing first with the plasticity component, it may be concluded that (14a) must be satisfied for all stress states because the yield function is convex, the plastic multiplier is non-negative and condition (32) is satisfied.

6.2. Damage-contact component

6.2.1. Open state

In the open state $\mathbf{C}_{\mathrm{lsf}}$ reduces to the form shown in Eq. (55), and the inequality (15) reduces to that shown in (56)

$$\mathbf{C}_{\mathrm{lsf}} = \left(\frac{1}{h_{\mathrm{c}}} - 1\right)\mathbf{C}_{\mathrm{L}} \quad \text{(for open state)} \tag{55}$$

$$[\mathbf{s}_i^{\mathrm{T}} \mathbf{C}_{\mathrm{L}} \mathbf{s}_i] \frac{-1}{h_{\mathrm{c}}^2} \left(\left(\frac{\mathrm{d}h_{\mathrm{c}}}{\mathrm{d}\zeta} \right) \dot{\zeta} + \left(\frac{\mathrm{d}h_{\mathrm{c}}}{\mathrm{d}\kappa} \right) \dot{\kappa} \right) = [\mathbf{s}_i^{\mathrm{T}} \mathbf{C}_{\mathrm{L}} \mathbf{s}_i] \frac{-1}{h_{\mathrm{c}}^2} \dot{h}_{\mathrm{c}} \geqslant 0 \tag{56}$$

$\mathbf{C}_{\mathrm{L}}$ is diagonal and positive for both options and therefore the term in square brackets must be non-negative. Also, $h_{\mathrm{c}} \geqslant 0$ (Eq. (16)), $\mathrm{d}h_{\mathrm{c}}/\mathrm{d}\zeta \leqslant 0$ and $\mathrm{d}h_{\mathrm{c}}/\mathrm{d}\kappa \leqslant 0$ (Eq. (24)), $\dot{h}_{\mathrm{c}} \leqslant 0$, $\dot{\zeta} \geqslant 0$ and $\dot{\kappa} \geqslant 0$, therefore inequality (56) must be satisfied.

6.2.2. Closed mode

In the closed state C_{lsf} reduces to C_{L} and thus inequality (15) is satisfied.

6.2.3. General interlock state case

As explained in Section 5, using option three for $\mathbf{D}_L$ resulted in $\mathbf{C}_{lsf}$ being symmetric and inequality (15) reducing to that shown in Eq. (54).

The sources for changes in $\mathbf{C}_{lsf}$, that are represented by $\dot{\mathbf{C}}_{lsf}$ in Eq. (54) are divided into two categories; firstly those resulting from changes in the proportion of damaged material that is in contact (H_f) and secondly those resulting from changes in the basic material components h_c and $(1-h_c)$.

Dealing with the first source changes; the total–local function (47) ensures that the local and global constitutive conditions are simultaneously satisfied and that there is a always a unique relationship between the global recoverable strains $(\boldsymbol{\varepsilon}-\boldsymbol{\varepsilon}_p)$ and the local strains $\mathbf{e}_i$ on each active POD i. H_{fi} is a function of $\mathbf{e}_i$ and the local stresses $\mathbf{s}_i$ are also functions of $\mathbf{e}_i$, therefore any closed cycle of the global strain tensor, that involves no plasticity and no damage, must return to the starting values of $\mathbf{s}_i$ and $\boldsymbol{\sigma}$. Thus, under these conditions, the model predicts zero dissipation for both symmetric or asymmetric forms of $\mathbf{C}_{lsf}$.

6.2.3.1. Plane-stress case with $\boldsymbol{C}_{lsf}$ option 3. With reference to the second source of changes, a two-dimensional plane stress case will be considered first, because for this case it proved possible to derive a compact analytical form to show that inequality (54) is satisfied by the present model for option three for which $E_n = E_\tau$. If the shear strain component is positive then $\mathbf{M}_x$ is equal to

$$\mathbf{M}_x = \begin{bmatrix} h_c & 0 \\ 0 & h_c \end{bmatrix} + \frac{H_f(1-h_c)}{1+m_g^2}\begin{bmatrix} m_g^2 & -m_g \\ -m_g & 1 \end{bmatrix} \tag{57}$$

It noted that that the final expression derived below does not depend on the sign of e_2.

Using the inverse of $\mathbf{M}_x$ from (57) in (27) gives the following form for $\mathbf{C}_{lsf}$

$$\mathbf{C}_{lsf} = \frac{1}{E_n}\begin{bmatrix} \dfrac{-h_c - h_c m_g^2 - H_f + H_f h_c}{(1+m_g^2)h_c(-h_c - H_f + H_f h_c)} & \dfrac{m_g H_f(h_c-1)}{(1+m_g^2)h_c(-h_c - H_f + H_f h_c)} \\ \dfrac{m_g H_f(h_c-1)}{(1+m_g^2)h_c(-h_c - H_f + H_f h_c)} & \dfrac{-h_c - h_c m_g^2 - m_g^2 H_f + m_g^2 H_f h_c}{(1+m_g^2)h_c(-h_c - H_f + H_f h_c)} \end{bmatrix} - \begin{bmatrix} \dfrac{1}{E_n} & 0 \\ 0 & \dfrac{1}{E_n} \end{bmatrix} \tag{58}$$

and

$$\frac{\partial \mathbf{C}_{lsf}}{\partial h_c} = \frac{1}{E_n}\begin{bmatrix} \dfrac{-1-m_g^2+H_f}{(1+m_g^2)h_c(-h_c - H_f + H_f h_c)} & \dfrac{m_g H_f}{(1+m_g^2)h_c(-h_c - H_f + H_f h_c)} \\ \dfrac{m_g H_f}{(1+m_g^2)h_c(-h_c - H_f + H_f h_c)} & \dfrac{-1-m_g^2+m_g^2 H_f}{(1+m_g^2)h_c(-h_c - H_f + H_f h_c)} \end{bmatrix} + \begin{bmatrix} -h_c - h_c m_g^2 - H_f + H_f h_c & m_g H_f(h_c-1) \\ m_g H_f(h_c-1) & -h_c - h_c m_g^2 - m_g^2 H_f + m_g^2 H_f h_c \end{bmatrix} \frac{2h_c + H_f - 2H_f h_c}{E_n(1+m_g^2)^2 h_c^2(-h_c - H_f + H_f h_c)^2} \tag{59}$$

Noting that here only changes in H_f due to changes in h_c are being considered,

$$\dot{\mathbf{C}}_{lsf} = \frac{\partial \mathbf{C}_{lsf}}{\partial h_c}\dot{h}_c \tag{60}$$

If $\dot{\mathbf{C}}_{lsf}$ is symmetric positive definite then the quadratic condition (54) must hold. This can be proved by showing that the matrix has all positive eigenvalues or, equivalently, by showing that it is an Hermitian matrix for which the minor principals are positive. For the present 2×2 matrix the latter may be summarized for a general matrix $\mathbf{A}$ by

$$\mathbf{A}_{11} > 0 \quad \text{and} \quad |\mathbf{A}| > 0.$$

From (59) and (60) the determinate of $\dot{\mathbf{C}}_{\mathrm{lsf}}$ may be shown to be the following

$$|\dot{\mathbf{C}}_{\mathrm{lsf}}| = \frac{-(\dot{h}_{\mathrm{c}})^2(H_{\mathrm{f}}-1)}{E_n^2 h_{\mathrm{c}}^2(-h_{\mathrm{c}}-H_{\mathrm{f}}+H_{\mathrm{f}}h_{\mathrm{c}})^2} \tag{61}$$

If H_{f} is less than unity, the determinate is always positive. Since this is zero when $H_{\mathrm{f}}=1$, which implies at least one zero eigenvalue and that the matrix is non-invertible, an upper limit of 0.995 is placed on H_{f}, as noted earlier.

From Eq. (59)

$$\frac{\partial \mathbf{C}_{\mathrm{lsf}}}{\partial h_{\mathrm{c}}}_{1,1}\dot{h}_{\mathrm{c}} = \frac{h_{\mathrm{c}}^2\left[(1-H_{\mathrm{f}})^2+m_g^2(1-H_{\mathrm{f}})\right]+2h_{\mathrm{c}}H_{\mathrm{f}}(1-H_{\mathrm{f}})+H_{\mathrm{f}}^2}{E_n(1+m_g^2)h_{\mathrm{c}}^2(H_{\mathrm{f}}h_{\mathrm{c}}-H_{\mathrm{f}}-h_{\mathrm{c}})^2}(-\dot{h}_{\mathrm{c}}) \tag{62}$$

and with $0<h_{\mathrm{c}}<1$, $0<H_{\mathrm{f}}<1$, $0<m_g<1$ and $\dot{h}_{\mathrm{c}}\leqslant 0$ this is always positive.

Thus, for the plane-stress case it is proved that the model satisfies the second law of thermodynamics with this symmetric form of $\mathbf{C}_{\mathrm{lsf}}$.

6.2.3.2. 3D case with $\boldsymbol{C}_{lsf}$ option 3. For the general 3D case it did not prove possible to derive an analytical form for the principal minors or the eigenvalues, however a compact form has been derived for $\mathbf{C}_{\mathrm{lsf}}$, which is given below, and this has been used to check the positive definiteness of $\dot{\mathbf{C}}_{\mathrm{lsf}}$.

$$\mathbf{C}_{\mathrm{lsf}} = \begin{bmatrix} m_g+\dfrac{h_{\mathrm{c}}}{\beta} & -\cos\theta & -\sin\theta \\ -\cos\theta & \dfrac{1}{m_g}-m_{\mathrm{r}}\sin^2\theta+\dfrac{h_{\mathrm{c}}}{\beta} & m_{\mathrm{r}}\cos\theta\sin\theta \\ -\sin\theta & m_{\mathrm{r}}\cos\theta\sin\theta & \dfrac{1}{m_g}-m_{\mathrm{r}}\cos^2\theta+\dfrac{h_{\mathrm{c}}}{\beta} \end{bmatrix}^{-1} \frac{1}{\beta E_n}-\mathbf{C}_{\mathrm{L}} \tag{63}$$

in which

$$m_{\mathrm{r}} = \frac{e_1}{\sqrt{e_2^2+e_3^2}}, \quad \theta = \arccos\left(\frac{e_1}{\sqrt{e_2^2+e_3^2}}\right) \quad \text{and} \quad \beta = \frac{(1-h_{\mathrm{c}})H_{\mathrm{f}}m_g}{1+m_g^2}$$

Using the following finite difference approximation, the normalized eigenvalues of $\dot{\mathbf{C}}_{\mathrm{lsf}}$ are given in Table 1 for a range of parameters.

$$\frac{\partial \mathbf{C}_{\mathrm{lsf}}(h_{\mathrm{c}})}{\partial h_{\mathrm{c}}}E_n\,\mathrm{sgn}(\dot{h}_{\mathrm{c}}) \approx \frac{\mathbf{C}_{\mathrm{lsf}}(h_{\mathrm{c}}+\Delta h_{\mathrm{c}})-\mathbf{C}_{\mathrm{lsf}}(h_{\mathrm{c}})}{\Delta h_{\mathrm{c}}}E_n\,\mathrm{sgn}(\dot{h}_{\mathrm{c}}) \tag{64}$$

noting that the derivative of $\mathbf{C}_{\mathrm{lsf}}$ is multiplied by the sign of $\dot{h}_{\mathrm{c}}$ so that the eigenvalues take the same sign as those of $\dot{\mathbf{C}}_{\mathrm{lsf}}$.

Table 1 shows that all three eigenvalues are always positive except when H_{f} is unity when, as predicted by the 2D study above, at least one eigenvalue is zero. Checks were performed for parameter values intermediate between the extreme values shown in the table and in all cases the eigenvalues were positive when the parameters were within the specified limits (e.g. $H_{\mathrm{f}}<1$). From this study it is concluded, though not formally proved, that the model with symmetric $\mathbf{C}_{\mathrm{lsf}}$ does always predict non-negative dissipation.

6.2.3.3. General case with $\boldsymbol{C}_{lsf}$ option 2. For the general 3D case with non-symmetric $\mathbf{C}_{\mathrm{lsf}}$ it did not prove possible to produce a compact analytical expression that proved that the model satisfies the second law of thermodynamics. Thus, numerical checks were performed for a series of strain paths in the interlock region in which both h_{c} and H_{f} were varied. The procedure adopted was to evaluate the work per unit volume (w) for a strain cycle, checking that the final total was positive. The strain paths used relatively small strain increments ($\Delta\boldsymbol{\varepsilon}$) and Eq. (65) was used to evaluate w.

Table 1
Normalised eigenvalues of $\dot{\mathbf{C}}_{\mathrm{lsf}}$

h_c	m_g	H_f	θ (°)	m_r	Eigen-values		
0.99	0.425	1	0	1	1.020	0	0.5183
0.01	0.425	1	0	1	1.000E4	0	2.1178
0.99	0.425	0.995	45	1	1.020	5.000E−3	0.5208
0.01	0.425	0.995	45	1	1.000E4	5.050E−3	2.1488
0.01	0.425	0.01	45	1	1.000E4	2.500E3	4.530E3
0.99	0.425	0.995	0	0.5	1.021	5.000E−3	0.3386
0.01	0.425	0.995	0	0.5	1.000E4	5.050E−3	0.7559
0.99	0.3	1	0	1	1.020	0	0.3604
0.01	0.3	1	0	1	1.000E4	0	0.8580
0.99	0.3	0.995	45	1	1.020	5.000E−3	0.3636
0.01	0.3	0.01	45	1	2.500E3	3.713E3	1.000E4
0.99	0.3	0.995	0	0.5	1.020	5.000E−3	0.2251
0.01	0.3	0.995	0	0.5	1.000E4	5.050E−3	0.3701
0.99	0.9	0.995	0	0.5	1.02031	5.000E−3	0.7075

$$w = \sum_{\text{increments}} \boldsymbol{\sigma}^{\mathrm{T}} \Delta\boldsymbol{\varepsilon} \tag{65}$$

Three paths are presented in Fig. 6 that include opening, closing, damaging and non-damaging sections in interlock mode. Paths 1 and 2 start and end with zero strain whereas path 3 has a closed loop from the strain identified as point B. In all cases the energy at the end of the closed cycle is greater than that at the start of the cycle. The material parameters used in the checks are shown in Table 2 but these paths were also checked with a range of different parameters which include elastic properties in the range 0.75–1.5 times the values shown, m_g in the range 0.3–0.9 and ε_0 in a range of 0.5–2 times the value shown. In all cases the paths showed positive dissipation.

6.3. Final remarks

This section has proved that for all cases, except the general interlock case, the model predicts dissipative behavior for both symmetric and asymmetric forms of local constitutive matrix. Furthermore, for the plane stress case, non-negative dissipation is also proved for the general interlock state with the symmetric form of local constitutive matrix. The corresponding three-dimensional idealization is also shown (though not formally proved) using a semi-analytical study to be dissipative. For the idealization with a non-symmetric local constitutive matrix, the interlock case did not prove amenable to analytical treatment and thus a numerical study was undertaken to assess whether the model is still dissipative. From this study it is concluded, albeit tentatively, that the model does satisfy the laws of thermodynamics even with an asymmetric local constitutive matrix, at least when using material properties suitable for normal structural concretes.

Overall the safest option from a purely theoretical view-point would be to use the form of the model with a symmetric local matrix, however, as will be shown in the next section, the asymmetric form produces results closer to those observed in experimental studies, and since the numerical study has also shown this form to be dissipative, this is the form used for the finite element simulations in the associated paper.

7. Single point stress–strain examples

A number of single point stress–strain path examples are given, which provide comparisons with test data. The numerical analyses were undertaken using a constitutive driver program in which the Craft model has been implemented. The material properties for each example are given in Table 3.

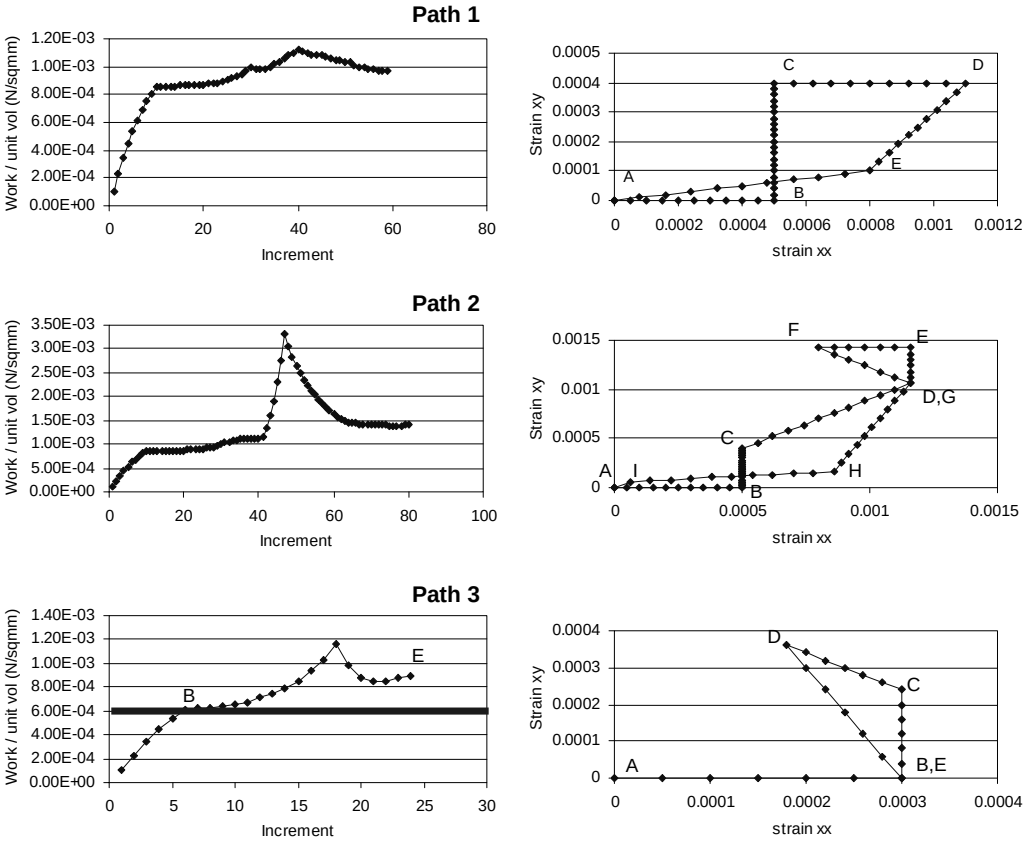

Fig. 6. Strain path work checks.

Table 2
Material properties used in test

E (N/mm^2)	ν	f_c (N/mm^2)	f_t (N/mm^2)	ε_c	ε_0	b_c	Z_0	ψ	m_g	m_{ful}
40 000	0.2	50	2.8	0.003	0.002	1.15	0.6	−0.1	0.425	10

The model has been developed with relatively few non-fixed material parameters, and each of these chosen parameters relates to a particular physical characteristic that could be measured experimentally. The non-standard parameters, along with a reference to section in which they are discussed, are as follows; b_r (3.2.3), Z_0 (3.2.2), ψ (3.2.3), m_g (3.1) and m_{ful} (3.1). The decisions to use only a few parameters, and to choose only those that could be directly related to a physical characteristic were made so that users of the model could understand the parameters and what they related to.

Example 1. In this example a comparison is made with the uniaxial tensile softening curve of Hordijk (1991). Hordijk's function is recognized to match well a wide range of data, and here the comparison is carried out for the data reported by van Mier (1997). In the simulation, an assumed fracture process zone of 60 mm is used and the elastic deformations are removed from the total to give the opening displacements. The comparison is shown in Fig. 7.

Table 3
Material properties used in examples

Example	E (kN/mm^2)	v	f_c (N/mm^2)	f_t (N/mm^2)	ε_c	ε_0	b_c	Z_0	ψ	m_g	m_{ful}
1	35	0.15	40	3.2	0.002	0.0027	1.15	0.5	−0.1	0.4	10
2	35	0.15	40	3.2	0.0022	0.0060	1.15	0.5	−0.1	0.4	10
3	30	0.15	29.5	2.7	0.0022	0.001	1.15	0.5	−0.1	0.38	20
4	35	0.18	32	2.4	0.0021	0.002	1.15	0.5	−0.2	0.4	10
5	37	0.15	46.9	3.0	0.0023	0.003	1.1	0.25	−0.3	0.4	10

Example 2. In this example a qualitative comparison is made with data from a test series on notched fracture specimens carried out by Reinhardt (1984). The specimens, illustrated in Fig. 8, had an effective area at the notch of 50×50 mm^2. The displacements were measured with extensometers with a gauge length of 35 mm. The data used here is from the narrow specimen tests designated LCLS (large compressive lower stress). It was assumed, in processing the numerical results, that the characteristic crack dimension was the gauge length used in the test. The limiting strain parameter ε_0 was computed from the opening displacement at the end of the softening curve (i.e. 0.21 mm) divided by the gauge length. The present model simulates secant reloading–unloading and full crack closure at zero axial strain (in this case), hence it was considered only necessary to show a single unloading reloading cycle in the numerical results. The results are shown in Fig. 9, in which the smooth transition to the closed state (See Eq. (22)) is just discernable from the graph.

Example 3. A comparison with the results from a pair of normal-shear tests undertaken by Walraven and Reinhardt (1981). The test specimens, which are illustrated in Fig. 10, each had a shear plane of 300×120 mm^2 and were tested in a stiff testing frame with external restraint bars used to control the crack opening. The tests were conducted with specified initial crack opening displacements, and in each case two tests were conducted with the same nominal openings. Once a crack had been formed to the required opening, a shear load was applied whilst the normal and shear displacements were monitored. The results of two experimental tests with initial opening displacements of 0.2 mm are shown in Fig. 11, along with the numerical results from the constitutive driver. The numerical predictions are not as accurate with the present model, which employs a simplified damage-contact crack-plane model, as those shown in Jefferson (2002b), but the model does simulate the stress free zone before contact, as well as the build up of shear and normal stresses reasonably.

Example 4. In this example comparison is made with data from a biaxial series of tests on plate type specimens by Kupfer et al. (1969). Uniaxial and biaxial compression tests are selected and plots given for both axial and lateral strains against the uniaxial compressive stress. Comparisons are shown in Fig. 12. It is noted that the graphs have been plotted in the compression positive convention of the experimental data.

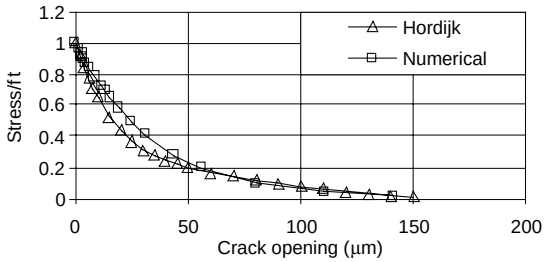

Fig. 7. Example 1. Uniaxial tension curve.

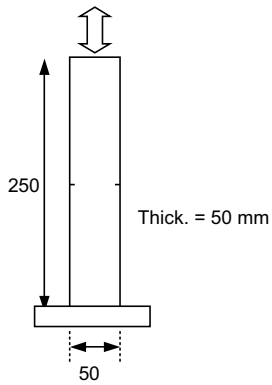

Fig. 8. Example 2. Reinhardt's cyclic testing arrangement.

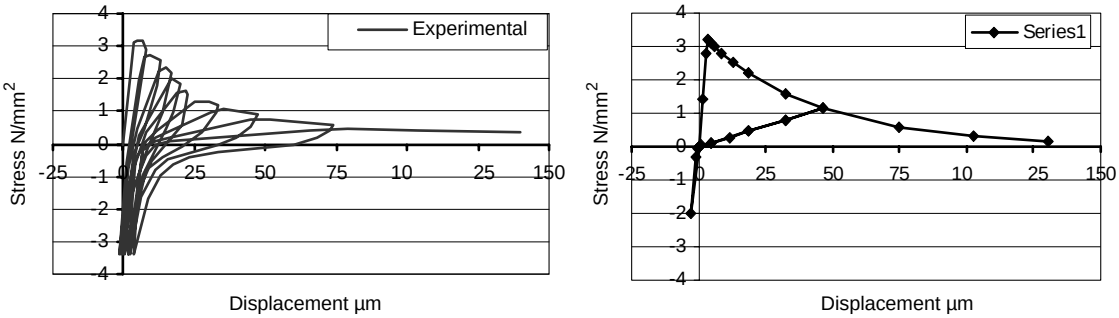

Fig. 9. Example 2. Uniaxial tension with crack opening and closing.

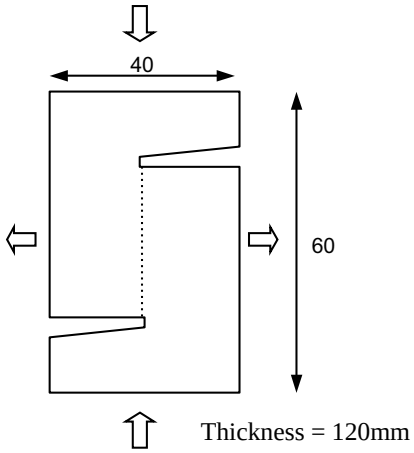

Fig. 10. Example 3. Walraven and Reinhardt's testing arrangement.

Example 5. In this example, comparison is made with data from a series of triaxial tests undertaken by Kotsovos and Newman (1979). Data from two triaxial tests are used for comparison, one with a confining stress of 35 N/mm^2 and the second with a confining stress of 70 N/mm^2. The comparisons are shown in

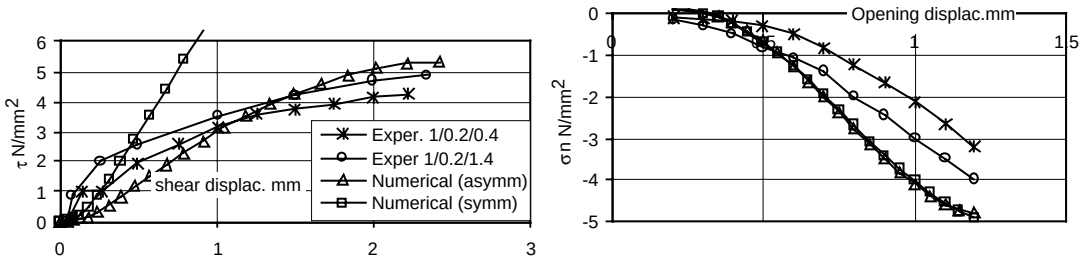

Fig. 11. Example 3. Walraven and Reinhardt's normal-shear tests.

Fig. 13. The graphs have again been plotted in the compression positive convention of the experimental data. It may seen from the comparisons that the model is less accurate at the higher confining stress at which hydrostatic crushing, not accounted for in this model, becomes significant. From these results it is suggested that, in triaxial cell terms, the model maintains reasonable accuracy up to confining stresses of one and half times the uniaxial compressive strength.

8. Conclusions and closing remarks

The model framework and associated conditions derived for ensuring thermodynamic validity are adequate for the development of a plastic directional-damage-contact model for concrete.

The new total–local consistency condition is effective at rigorously maintaining the local and global constitutive relationships as well as the stress transformation relationships.

The relatively simple functions used in the local POD model allow the accurate simulation of direct tension fracture behavior. Furthermore, the incorporation of a contact model on damaged PODs enables crack closure, shear contact and aggregate interlock behavior to be simulated with reasonable accuracy.

The frictional hardening plasticity component is adequate for simulating the compressive behavior of concrete up to confining stresses of approximately 1.5 times the uniaxial compressive strength (in triaxial cell terms).

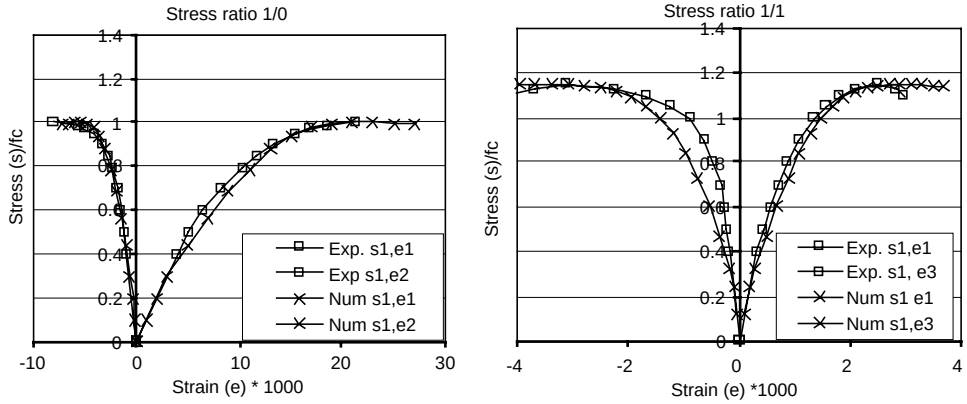

Fig. 12. Example 4. Compressive test data from Kupfer, Hilsdorf and Rusch.

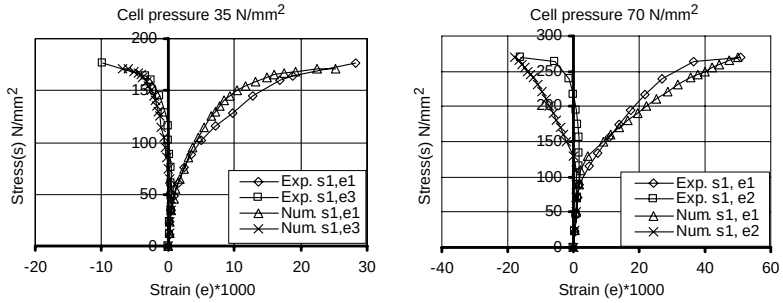

Fig. 13. Example 5. Triaxial test data from Kotsovos and Newman.

It has been proved for certain restricted cases that the model satisfies the second law of thermodynamics, and furthermore for other cases it has been demonstrated that for parameter ranges typical for structural concrete the model does always predict non-negative dissipation.

Two particular future developments to the model are planned, as follows

- an optional closed yield surface with curved meridians which is able to simulate crushing effects at high triaxial confinements
- frictional behavior in the crack plane model (as in Jefferson, 2002b) to simulate crack unloading/reloading hysteretic effects, although again this is intended to be a model option.

Acknowledgements

I would like to thank the Royal Society (UK) for supporting this work and the finite element software company FEA Ltd. for their support, help and enthusiasm for the work.

Appendix A

This appendix presents details of the local and global stress and strain vectors, transformation rules and elastic constitutive matrices.

The POD, along with its defining local and global coordinate systems, are shown in Fig. 14.

The local stresses are related to global by the following transformation

$$\mathbf{s}_i = \mathbf{N}_i \boldsymbol{\sigma} \tag{A.1}$$

where i presents the POD number.

$$\mathbf{s} = [\, s_\mathrm{r} \quad s_\mathrm{s} \quad s_\mathrm{t} \,]^\mathrm{T} \quad \text{and} \quad \sigma = [\, \sigma_{xx} \quad \sigma_{yy} \quad \sigma_{zz} \quad \tau_{xy} \quad \tau_{yz} \quad \tau_{xz} \,]^\mathrm{T}$$

$$\mathbf{N} = \begin{bmatrix} r_{\mathrm{d}1}^2 & r_{\mathrm{d}2}^2 & r_{\mathrm{d}3}^2 & 2r_{\mathrm{d}1}r_{\mathrm{d}2} & 2r_{\mathrm{d}2}r_{\mathrm{d}3} & 2r_{\mathrm{d}1}r_{\mathrm{d}3} \\ s_{\mathrm{d}1}^2 & s_{\mathrm{d}2}^2 & s_{\mathrm{d}3}^2 & 2s_{\mathrm{d}1}s_{\mathrm{d}2} & 2s_{\mathrm{d}2}s_{\mathrm{d}3} & 2s_{\mathrm{d}1}s_{\mathrm{d}3} \\ t_{\mathrm{d}1}^2 & t_{\mathrm{d}2}^2 & t_{\mathrm{d}3}^2 & 2t_{\mathrm{d}1}t_{\mathrm{d}2} & 2t_{\mathrm{d}2}t_{\mathrm{d}3} & 2t_{\mathrm{d}1}t_{\mathrm{d}3} \end{bmatrix}$$

$r_{\mathrm{d}1}$, $r_{\mathrm{d}2}$, $r_{\mathrm{d}3}$ are the x, y, z components of the unit vector $\mathbf{r}_\mathrm{d}$, normal to the POD surface, and similarly $\mathbf{s}_\mathrm{d}$ and $\mathbf{t}_\mathrm{d}$ are the in-plane vectors. $\mathbf{s}_\mathrm{d}$ is generated in the same way that Hasegawa (1995) generated shear directions for micro-planes, in that the directions are chosen orthogonal to $\mathbf{r}_\mathrm{d}$ and to each of the reference axes in turn,

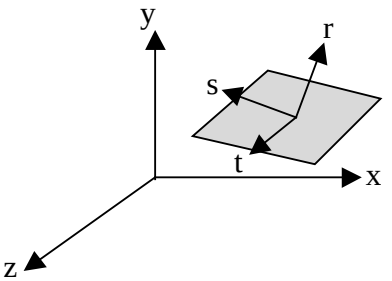

Fig. 14. POD local and global coordinate systems.

i.e. for plane 1 $\mathbf{s}_d$ is orthogonal to z, for plane 2 $\mathbf{s}_d$ is orthogonal to y etc. $\mathbf{t}_d$ is then made orthogonal to $\mathbf{r}$ and $\mathbf{s}$.

When applied as direction subscripts to $\mathbf{e}$ and $\mathbf{s}$, the d subscript on $\mathbf{r}_d$, $\mathbf{s}_d$ and $\mathbf{t}_d$ is dropped.

The local stresses are related to the normal and principal shearing stresses on the POD as follows,

$$\sigma_n = s_r \quad \text{and} \quad \tau = (s_s^2 + s_t^2)^{1/2} \tag{A.2}$$

Effective local strain and total global strain vectors are as follows

$$\mathbf{e} = \begin{bmatrix} e_r & e_s & e_t \end{bmatrix}^T \quad \text{and} \quad \boldsymbol{\varepsilon} = \begin{bmatrix} \varepsilon_{xx} & \varepsilon_{yy} & \varepsilon_{zz} & \gamma_{xy} & \gamma_{yz} & \gamma_{xz} \end{bmatrix}^T \tag{A.3}$$

The global stress–elastic strain relationships are given by

$$\boldsymbol{\sigma} = \mathbf{D}_e \boldsymbol{\varepsilon}_e \tag{A.4}$$

$$\boldsymbol{\varepsilon}_e = \mathbf{C}_e \boldsymbol{\sigma} \tag{A.5}$$

in which $\mathbf{D}_e$ and $\mathbf{C}_e$ are the standard 6×6 matrices of elastic constants in stiffness and compliance form respectively.

The local elastic relationships are given by

$$\mathbf{s} = \mathbf{D}_L \mathbf{e}_e \quad \text{and} \quad \mathbf{e}_e = \mathbf{C}_L \mathbf{s} \tag{A.6}$$

where

$$\mathbf{D}_L = \begin{bmatrix} E_n & 0 & 0 \\ 0 & E_\tau & 0 \\ 0 & 0 & E_\tau \end{bmatrix} \quad \text{and} \quad \mathbf{C}_L = \begin{bmatrix} 1/E_n & 0 & 0 \\ 0 & 1/E_\tau & 0 \\ 0 & 0 & 1/E_\tau \end{bmatrix}$$

References

Abu-Lebeh, M., Voyiadjis, G.Z., 1993. Plasticity-damage model for concrete under cyclic multiaxial loading. J. Eng. Mech. ASCE 119 (7), 1465–1484.

ACI Committee 446, 1998. Finite element analysis in concrete structures. ACI report 446.3R-97.

Armero, F., Oller, S., 2000. A general framework for continuum damage models. I: Infinitesimal plastic damage models in stress space. Int. J. Solids Struct. 37, 7409–7436.

ASCE Task Committee on Finite Element Analysis of Reinforced Concrete Structures, 1982. Finite element analysis of reinforced concrete structures. ASCE.

Bazant, Z.P., Caner, F.C., Carol, I., Adley, M.D., Akers, S.A., 2000. Micro-plane model M4 for concrete. I: Formulation with work conjugate deviatoric stress. J Eng. Mech. ASCE 126 (9), 944–953.

Bazant, Z.P., Jirasek, M., 2002. Nonlocal integral formulations of plasticity and damage: Survey of progress. J. Eng. Mech. ASCE 128 (11), 1119–1149.
Bazant, Z.P., Oh, B.H., 1983. Crack band theory for fracture in concrete. Mater. Struct. 16, 155–177.
Buyukozturk, O., 1977. Non-linear analysis of reinforced concrete. Comput. Struct. 7, 149–156.
Carol, I., Jirasek, M., Bazant, Z.P., 2001a. A thermodynamically consistent approach to micro-plane theory. Part 1: Free energy and consistent microplane stresses. Int. J. Solids Struct. 38, 2921–2931.
Carol, I., Rizzi, E., Willam, K., 2001b. On the formulation of anisotropic elastic degradation. I: Theory based on a pseudo-logarithmic damage tensor rate, and II: Generalized pseudo-Rankine model for tensile damage. Int. J. Solids Struct. 38, 491–546.
Cervera, M., Hinton, E., Hassan, O., 1987. Non-linear analysis of reinforced concrete plate and shell structures using 20-noded isoparametric brick elements. Comput. Struct. 25 (6), 845–869.
Comi, C., Perego, U., 2001. Fracture energy based bi-dissipative damage model for concrete. Int. J. Solids Struct. 38, 6427–6454.
Crisfield, M.A., Wills, J., 1989. The analysis of reinforced-concrete panels using different concrete models. J. Eng. Mech. ASCE 15 (3), 578–597.
de Borst, R., Nauta, P., 1985. Non-orthogonal cracks in a smeared finite element model. Eng. Comput. 2, 35–46.
de Borst, R., 1986. Computational aspects of smeared crack analysis. In: Hinton, E., Owen, D.R.J. (Eds.), Computational Modeling of Reinforced Concrete. Pineridge Press, Swansea, pp. 44–83.
di Prisco, M., Mazars, J., 1996. Crush-crack: a non-local damage model for concrete. Mech. Cohes. Frict. Mater. 1, 321–347.
Ekh, M., Runesson, K., 2000. Bifurcation results for plasticity coupled to damage with MCR-effect. Int. J. Solids Struct. 37, 1975–1996.
Este, G., Willam, K., 1994. Fracture energy formulation for inelastic behavior of plain concrete. J. Eng. Mech. ASCE 120 (9), 1983–2011.
Feenstra, P.H., de Borst, R., 1995. A plasticity model and algorithm for mode-I cracking in concrete. Int. J. Numer. Meth. Eng. 38, 2509–2529.
Han, D.J., Chen, W.F., 1987. Constitutive modeling in the analysis of concrete structures. J. Eng. Mech. ASCE 113 (4), 577–593.
Hansen, N.R., Schreyer, H.L., 1994. A thermodynamically consistent framework for theories of elastoplasticity coupled with damage. Int. J. Solids Struct. 31 (3), 359–389.
Hasegawa, T., 1995. Enhanced micro-plane concrete model. In: Proceedings of FAMCOS2. Wittmann, F.H. Aedificatio, Germany, pp. 857–870.
Hordijk, D.A., 1991. Local approach to fatigue of concrete. Ph.D. Thesis, Delft University of Technology, The Netherlands.
Jefferson, A.D., 2002a. A constitutive model for aggregate interlock on formed crack planes. Int. J. Numer. Anal. Meth. Geomech. 26, 1–21.
Jefferson, A.D., 2002b. Tripartite cohesive crack model. J. Eng. Mech. ASCE 128 (6), 644–653.
Jefferson, A.D., 2003. Craft—a plastic-damage-contact model for concrete. II. Model implementation with implicit return mappings algorithm and consistent tangent matrix. Int. J. Solids Struct. in this issue.
Karihaloo, B.L., Jefferson, A.D., 2001. Looking into concrete. Mag. Concr. Res. 53 (2), 135–147.
Klisinski, M., Mroz, Z., 1988. Description of inelastic deformation and degradation of concrete. Int. J. Solids Struct. 24 (4), 391–416.
Kotsovos, M.D., Newman, J.B., 1979. A mathematical description of the deformable behavior of concrete under complex loading. Mag. Concr. Res. 31, 77–90.
Krajcinovic, D., 1996. Damage Mechanics. Elsevier.
Kroplin, B., Weihe, S., 1997. Aspects of fracture induced anisotropy. In: Proceedings of the 5th International Conference on Computational Plasticity (COMPLAS5), Barcelona. pp. 255–279.
Kupfer, H.B., Hilsdorf, H.K., Rusch, H., 1969. Behavior of concrete under biaxial stresses. J. ACI 66 (8), 656–666.
Lee, J., Fenves, G.L., 1998. Plastic-damage model for cyclic loading of concrete structures. J. Eng. Mech. ASCE 124, 892–900.
Lubiner, J., Oliver, J., Oller, S., Onate, E., 1989. A plastic-damage model for concrete. Int. J. Solids Struct. 25 (3), 299–326.
Luccioni, B., Oller, S., Danesi, R., 1996. Coupled plastic-damaged model. Comput. Meth. Appl. Mech. Eng. 129, 81–89.
Meschke, G., Lackner, R., Mang, H.A., 1998. An anisotropic elastoplastic-damage model for plain concrete. Int. J. Numer. Meth. Eng. 42, 703–727.
Oliver, J., 1990. A consistent characteristic length for smeared crack models. Int. J. Numer. Meth. Eng. 28, 461–474.
Ortiz, M., 1985. A constitutive theory for the inelastic behavior of concrete. Mech. Mater. 4, 67–93.
Ortiz, M., Simo, J.C., 1986. An analysis of a new class of integration algorithms for elastoplastic constitutive relations. Int. J. Numer. Meth. Eng. 23, 353–366.
Owen, D.R.J., Figueriras, J.A., Damjanic, F., 1983. Finite element analysis of reinforced and prestressed concrete structures including thermal loading. Comput. Meth. Appl. Mech. Eng. 41, 323–366.
Ožbolt, J., Li, Y.-J., Koar, I., 2001. Micro-plane model for concrete with relaxed kinematic constraint. Int. J. Solids Struct. 38, 2683–2711.
Petrangeli, M., Ozbolt, J., 1996. Smeared crack approaches—Material modeling. J. Eng. Mech. ASCE 122 (6), 545–554.
Reinhardt, H.W., 1984. Fracture mechanics of an elastic softening material like concrete. Heron 29 (2), 1–42.

Rots, J.G., 1988. Computational modeling of concrete fracture. Ph.D. Thesis, Delft University of Technology, The Netherlands.
Saenz, L.P., 1964. Discussion of 'Equation for the stress–strain curve for concrete' by Desai and Krishnan. J. ACI 61 (9), 1229–1235.
Simo, J.C., Ju, J.W., 1987. Relative displacement and stress based continuum damage models. I: Formulation. Int. J. Solids Struct. 23 (7), 821–840.
Simo, J.C., Taylor, R.L., 1985. Consistent tangent operators for rate independent elasto-plasticity. Comput. Meth. Appl. Mech. Eng. 48, 101–118.
Walraven, J.C., Reinhardt, H.W., 1981. Theory and experiments on the mechanical behavior of cracks in plain and reinforced concrete subjected to shear loading. Heron 26 (1A).
Weihe, S., Kroplin, B., de Borst, R., 1998. Classification of smeared crack models based on material and structural properties. Int. J. Solids Struct. 35 (12), 1289–1308.
Willam, K., Warnke, E., 1975. Constitutive models for triaxial behavior of concrete. In: Proceedings of the International Association of Bridge Structure Engineering, Report 19, Zurich, Switzerland. pp. 1–30.
van Mier, J.G.M., 1997. Fracture processes of concrete. CRC Press, Boca Raton, FL.
Yang, B.L., Dafalias, Y.F., Hermann, L.R., 1985. A bounding surface plasticity model for concrete. J. Eng. Mech. ASCE 111 (3), 359–380.